

This item was submitted to [Loughborough's Research Repository](#) by the author.
Items in Figshare are protected by copyright, with all rights reserved, unless otherwise indicated.

Deformation characteristics in micromachining of single crystal 6H-SiC: Insight into slip systems activation

PLEASE CITE THE PUBLISHED VERSION

<https://doi.org/10.1017/jmech.2019.63>

PUBLISHER

Cambridge University Press (CUP)

VERSION

AM (Accepted Manuscript)

PUBLISHER STATEMENT

This paper was accepted for publication in the journal Journal of Mechanics and the definitive published version is available at <https://doi.org/10.1017/jmech.2019.63>

LICENCE

CC BY-NC-ND 4.0

REPOSITORY RECORD

Pang, KH, Rongxin Zhou, and Anish Roy. 2020. "Deformation Characteristics in Micromachining of Single Crystal 6h-sic: Insight into Slip Systems Activation". Loughborough University.
<https://hdl.handle.net/2134/13607675.v1>.

DEFORMATION CHARACTERISTICS IN MICROMACHINING OF SINGLE CRYSTAL 6H-SiC: INSIGHT INTO SLIP SYSTEMS ACTIVATION

K. H. Pang

*Surrey Space Centre,
University of Surrey
Guildford, GU2 7XH, The UK.*

R. Zhou

*Wolfson School of Mechanical, Electrical and Manufacturing Engineering
Loughborough University
Loughborough, LE11 3TU, The UK.*

A. Roy*

*Wolfson School of Mechanical, Electrical and Manufacturing Engineering
Loughborough University
Loughborough, LE11 3TU, The UK.*

ABSTRACT

Silicon carbide (SiC) is ideally suitable as a sensor material in harsh environments. Despite the brittleness in the macroscopic scale, plasticity in SiC is observed at small component length-scales. Previous nanoindentation based study combining experiment and numerical approaches of single-crystal 6H-SiC has shown that slip activation is rather complex, and that non-basal slip could potentially dominate the plastic deformation behaviour. In this study, we investigated the local deformation response evolution of shear strain directly under and in the vicinity of the indenter tip. The results show the pyramidal slip families contribute significantly to the deformation process.

Keywords: Nanoindentation, Crystal plasticity, Silicon carbide, Finite element analysis.

1. INTRODUCTION

Silicon carbide (SiC) is a promising candidate for sensors components and MEMS devices deployed in harsh-environments due to its excellent high-temperature tolerance, mechanical robustness, and chemical stability at high temperatures. Thus, components made from SiC are ideally suited for technically demanding applications where components are subjected to high-temperature [1], radiation [2], and corrosive environments [3].

SiC is known to exist in a variety of crystalline structure. Interestingly, the difference is observed in the stacking sequence in one-dimension only. These variants are known as polytypes of SiC with over 100 polytypes of SiC being reported in the literature. Amongst these, 6H-SiC is a polytype exhibiting hexagonal symmetry and is popular in microelectronic devices as it can be manufactured reliably in bulk [4]. Unfortunately, its superior mechanical and chemical characteristics is a hindrance in manufacturing components via machining, especially at small length scales. Interestingly, SiC is mechanically brittle in the macroscale, but, it demonstrates ductile plasticity at small length-scales. Thus, a thorough understanding of the deformation behaviour at a small length scale is warranted to facilitate fabrication of the small-sized component.

Over the years, significant research efforts in understanding this ductile behaviour in the micro-machining of silicon (Si) and SiC components have been made, such as in abrasive machining [5], nano-scratching [6-8] and single point diamond turning (SPDT) [9,10]. The small-scale ductility in SiC is generally attributed to two possible reasons. One school of thought suggest that high-pressure phase transformation (HPPT) as the main reason for the material

* A Roy (A.Roy3@lboro.ac.uk)

removal in the ductile regime during the SPDT process [11]. TEM based diffraction study shows no halo rings which implies that an amorphous structure was not present. Conversely, studies on diamond turning [12, 13] and nanoindentation [14–17] indicated that the deformation is facilitated primarily by dislocation-assisted plasticity. Datye et. al [17] perform nanoindentation to quantify the hardness and effective modulus at four different crystallographic orientations experimentally and numerically through crystal plasticity modelling. The study concludes that the weak anisotropy in 6H-SiC is due to the basal slip-system dominating plastic deformation. However, other studies contradict this finding [8,18] by demonstrating that slip on all slip systems (however small) contribute to the overall deformation which cannot be ignored.

Here, we investigate the plastic deformation behaviour, in particular, the slip activities in monocrystalline 6H-SiC induced by nanoindentation. A numerical model is developed that is shown to accurately capture the essential deformation mechanisms in 6H-SiC.

2. CLASSICAL CRYSTAL PLASTICITY THEORY

Crystal plasticity has been successfully incorporated to study the deformation mechanism of a host of crystalline materials including the deformation in hexagonal closed packed (HCP) single crystalline metals [19–21]. The approach was employed extensively to simulate a number of small scales studies such as nanoindentation experiment [22, 23]. The technique has also been extended to model the micromachining process in single and polycrystalline materials. The theory and formulation of crystal plasticity employed in the analysis here are discussed in detail in [24]. For completeness, we provide a concise description of the theory.

The deformation gradient, \mathbf{F} , is given by,

$$\mathbf{F} = \mathbf{F}_e \mathbf{F}_p, \quad (1)$$

where the subscripts ‘e’ denotes the elastic part and ‘p’ denotes the plastic part. Temporal evolution of the deformation gradient, $\dot{\mathbf{F}}$, is derived as,

$$\dot{\mathbf{F}} = \dot{\mathbf{F}}_e \mathbf{F}_p + \mathbf{F}_e \dot{\mathbf{F}}_p. \quad (2)$$

The velocity gradient \mathbf{L} in the current state is

$$\mathbf{L} = \dot{\mathbf{F}}_e \mathbf{F}_e^{-1} + \mathbf{F}_e (\dot{\mathbf{F}}_p \mathbf{F}_p^{-1}) \mathbf{F}_e^{-1} = \mathbf{L}_e + \mathbf{L}_p. \quad (3)$$

The plastic part of the velocity gradient, \mathbf{L}_p , is determined from the cumulative evolution of shear strain on individual slip system,

$$\mathbf{L}_p = \sum_{\alpha=1}^N \dot{\gamma}^{(\alpha)} \mathbf{s}^{(\alpha)} \otimes \mathbf{m}^{(\alpha)}, \quad (4)$$

where $\dot{\gamma}^{(\alpha)}$ is the slipping rate of the α^{th} slip system which ranges from 1 to N , unit vectors $\mathbf{s}^{(\alpha)}$ is the slip direction and $\mathbf{m}^{(\alpha)}$ is the normal to the slip plane in the current configuration. The velocity gradient can also be represented as,

$$\mathbf{L} = \mathbf{D} + \mathbf{W} = (\mathbf{D}_e + \mathbf{W}_e) + (\mathbf{D}_p + \mathbf{W}_p) = \dot{\mathbf{F}}_e \mathbf{F}_e^{-1} + \sum_{\alpha=1}^N \dot{\gamma}^{(\alpha)} \mathbf{s}^{(\alpha)} \otimes \mathbf{m}^{(\alpha)} \quad (5)$$

where, \mathbf{D} , is the rate of deformation tensor and, \mathbf{W} , is the antisymmetric spin tensor.

The constitutive law employed here is based on the work of Huang [25] and is expressed as the relationship between the Jaumann rate of the Cauchy stress, $\overset{\nabla}{\boldsymbol{\sigma}}$, and the elastic part of the rate of deformation tensor, \mathbf{D}_e ,

$$\overset{\nabla}{\boldsymbol{\sigma}} + \boldsymbol{\sigma}(\mathbf{I} : \mathbf{D}_e) = \mathbf{C} : \mathbf{D}_e, \quad (6)$$

where, \mathbf{I} is the identity tensor, \mathbf{C} is the fourth-order possibly anisotropic elastic moduli tensor. The Jaumann stress rate is determined from,

$$\overset{\nabla}{\boldsymbol{\sigma}} = \dot{\boldsymbol{\sigma}} - \mathbf{W}_e \boldsymbol{\sigma} + \boldsymbol{\sigma} \mathbf{W}_e. \quad (7)$$

On the slip system, α , the resolved shear stress, $\tau^{(\alpha)}$, is determined from,

$$\tau^{(\alpha)} = \text{sym}(\mathbf{s}^{(\alpha)} \otimes \mathbf{m}^{(\alpha)}) : \boldsymbol{\sigma}. \quad (8)$$

The slipping rate, $\dot{\gamma}^{(\alpha)}$, is determined by the corresponding resolved shear stress, $\tau^{(\alpha)}$, with a power-law relation after Hutchinson [26],

$$\dot{\gamma}^{(\alpha)} = \dot{\gamma}_0 \left| \frac{\tau^{(\alpha)}}{g^{(\alpha)}} \right|^n \text{sgn}(\tau^{(\alpha)}), \quad (9)$$

where, n is the rate-sensitivity exponent, $g^{(\alpha)}$ is the slip resistance on the specific slip system, and $\dot{\gamma}_0$ is the reference shear-rate. The evolution of strength, $\dot{g}^{(\alpha)}$, is determined from,

$$\dot{\gamma}^{(\alpha)} = \sum_{\beta=1}^N h_{\alpha\beta} |\dot{\gamma}^{(\beta)}|, \quad (10)$$

where, $h_{\alpha\beta}$ is the slip hardening modulus. A relation for the self ($h_{\alpha\alpha}$) and latent hardening ($h_{\alpha\beta}$) moduli are obtained from the prior work of Peirce et al. [27] and Asaro [28, 29],

$$h_{\alpha\alpha} = h_0 \operatorname{sech}^2 \left| \frac{h_0 \gamma}{\tau_s - \tau_0} \right|, \quad (11)$$

$$h_{\alpha\beta} = q h_{\alpha\alpha} (\alpha \neq \beta)$$

where, h_0 is the initial hardening modulus and the upper limit of equation (11), q the latent hardening ratio, τ_0 the initial critical resolved shear stress (CRSS) and τ_s the saturation stress.

The cumulative shear strain on all slip systems, γ , is defined as,

$$\gamma = \sum_{\alpha} \int_0^t |\dot{\gamma}^{(\alpha)}| dt. \quad (12)$$

3. FINITE ELEMENT MODEL

The crystal plasticity theory was incorporated in a general-purpose finite element (FE) modelling package Abaqus/Explicit 6.14 as a user-defined material subroutine (VUMAT). A schematic of the nanoindentation process on two chosen crystallographic orientations is shown in Figure 1 (a), (b). Orientation 1 is defined to be such that the loading direction was perpendicular to the basal plane (0001) (Figure 1(a)). The second orientation (Orientation 2) was chosen such that the loading direction was inclined at 45° to the basal plane (Figure 1(b)). Physical experiments were conducted to obtain load-displacement experimental data. The FE model used in the study is shown in Figure 1 (c). The domain was meshed with 8-node linear isoparametric elements (C3D8) available in ABAQUS. A higher density mesh was used in the vicinity of the indented area to improve numerical accuracy. The total element number in the model was $\sim 23 \times 10^3$. The mesh density was deemed adequate yielding a good balance between accuracy and computational efficiency as per mesh convergence studies performed elsewhere [18]. A Berkovich indenter was used for the simulation which has a tip radius of 400 nm with a half-angle of 65.27°. It was assumed not to deform during the experiment. Hence an analytical rigid constraint was assigned to the indenter in the numerical model. The simulation was conducted by assigning a displacement of 207 nm in the negative y-direction (see Figure 1(c)). The loading time was 10 s which approximately correspond to a peak load of 30 mN. Next, an unloading step was performed by retracting the indenter which was completed in 5 s. A 6 cores high-performance computing cluster was used for all the simulations in the current study, and the computation took about 10 hours to complete. Five sets of slip families, namely, basal, prismatic, pyramidal $\langle a \rangle$, pyramidal $\langle c+a \rangle$ 1st order and pyramidal $\langle c+a \rangle$ 2nd order available in HCP crystals are considered in the study. Details of model implementation and slip systems considered in this study are available in [18]. The simulated results were calibrated against experimental data. Table 1 list all the calibrated material parameters of the monocrystalline 6H-SiC.

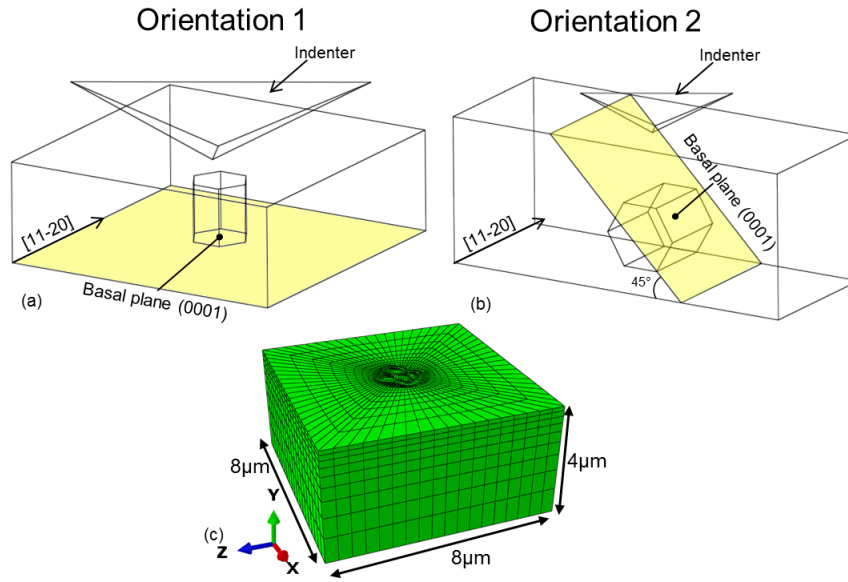


Figure 1 Indentation direction with respect to crystallographic orientations in (a) orientation 1, (b) orientation 2 and (c) Finite-element model for simulation

Table 1 Material parameters of monocrystalline 6H-SiC [18]

Parameter	Definition	Values	Unit
C_{11}	Elastic constants	325	GPa
C_{12}		60	GPa
C_{13}		34	GPa
C_{33}		367	GPa
C_{44}		109	GPa
$\dot{\gamma}_0$	Reference slipping rate	0.01	s^{-1}
n	Rate-sensitivity exponent	80	-
τ_0	Basal and Prismatic	Initial CRSS	9.85 GPa
τ_s		Saturated stress	15 GPa
h_0		Initial hardening modulus	9 GPa
τ_0	Pyramidal <a>, Pyramidal <c+a> 1 st and 2 nd order	Initial CRSS	11 GPa
τ_s		Saturated stress	15 GPa
h_0		Initial hardening modulus	9 GPa

4. RESULTS AND DISCUSSION

4.1 Force-displacement curves

A comparison of the experimental and numerical force-displacement response is shown in Figure 2 for orientation 1 and 2. The experimental data were obtained from a prior study [18]. Parameter calibration was accomplished by performing a sensitivity analysis on the hardening parameters (i.e. initial CRSS, saturated stress and initial hardening modulus) as well as the elastic constant to match with the maximum load, the slope of the initial portion of the unloading curve and the residual depth after full unloading. The numerical results match reasonably with the experimental data. For orientation 1, the simulated result matches closely as the model was calibrated based on this experiment. For orientation 2, the numerical results are predictive. The results showed a slight deviation between the experimental and simulation results in the loading-unloading curves at high loads. However, the residual displacement (the depth where the indenter completely unloaded) show a close correspondence between experiments and numerical results.

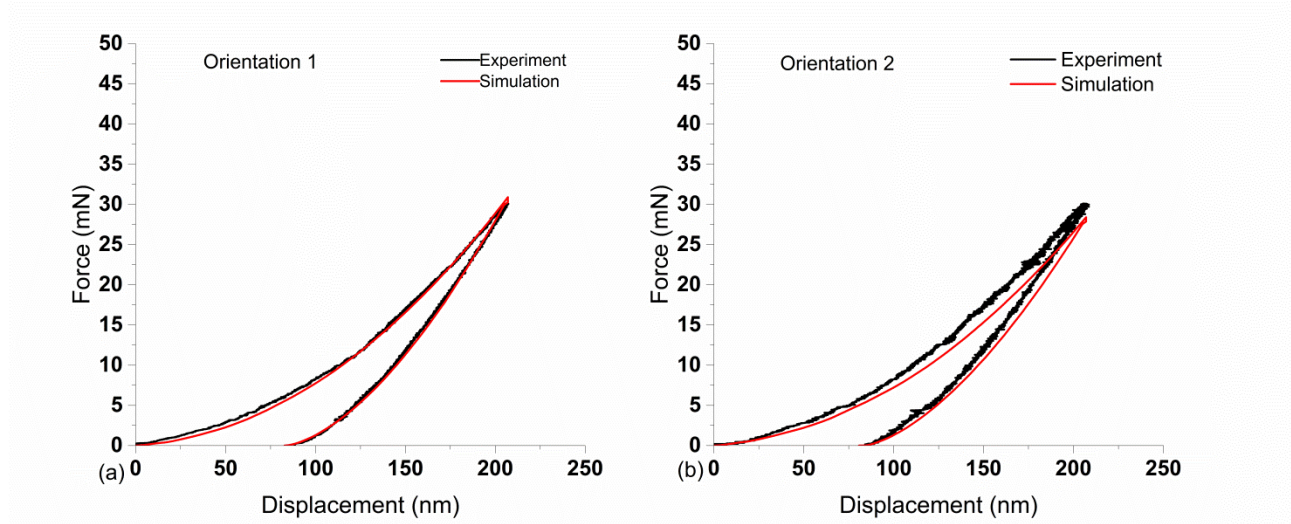


Figure 2 Comparison of force-displacement response at (a) orientation 1 and (b) orientation 2

4.2 Slip activation

Prior study in [18] suggests that the local plastic deformation in the nanoindentation process could potentially be dominated by the slip in the pyramidal $\langle c+a \rangle$ families. As a result, considering all slip families (instead of the basal system only) is important. Here, the local shear strain evolution in the vicinity of the indentation imprint was studied. Figure 3 shows the contour plot of the cumulated residual shear strain, i.e. after the unloading step. Here, four locations are selected for further analysis of the shear strain evolution for both orientations. First, we choose the location immediately under the indenter tip as we expect maximum compressive stresses to be imposed here. This position is labelled as 'Tip' in our analysis. Next, we choose the centre point of the three edges/sides of the indenter geometry which corresponds to the centre of the residual impression in the material. This is labelled as Location 1, 2 and 3 in the analysis. These three locations are chosen to demonstrate the anisotropy of the underlying deformation.

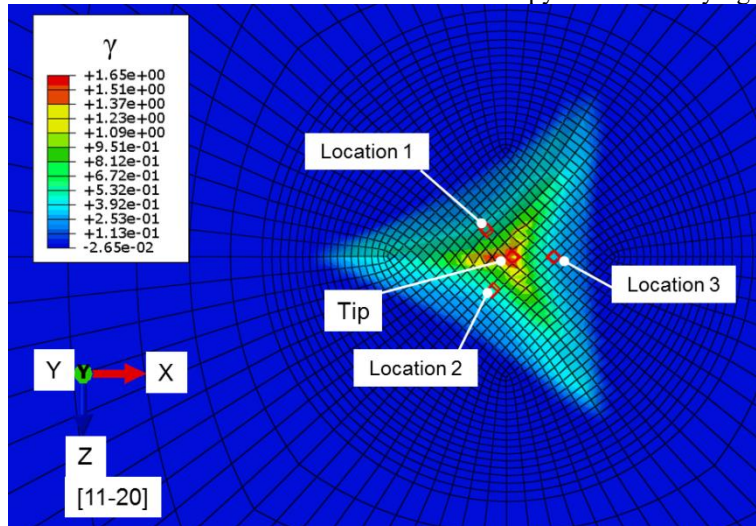


Figure 3 Cumulative shear strain overall slip system. Four locations indicating the area underneath the tip (Tip) and in

the centre point of the three sides of the impression (Location 1-3) were studied.

Figure 4 shows the evolution of shear strain in each of the five slip families during the loading step at the Tip location in orientation 1 and 2. For both orientations, 1st order pyramidal $\langle c+a \rangle$ system show the highest level of slip activity and not the basal slip system alone. The 2nd order pyramidal $\langle c+a \rangle$ also show significant slip activity with minor basal slip activation in orientation 1 (Figure 4 (a)). This is due to the fact that locally the basal plane is under nominally uniaxial compression at the tip location. As a result, the basal slip activation is insignificant. By a similar argument pyramidal $\langle c+a \rangle$ is oriented favourably to accommodate slip during deformation. In orientation 2, we observe significant activation of the basal family especially towards the end of the load step (Figure 4(b)). This agrees with studies in [17] that show that a high level of slip activation was expected in this orientation immediately below the indenter tip. Interestingly, the pyramidal $\langle c+a \rangle$ family contributes substantially to slip primarily due to the orientation of the material.

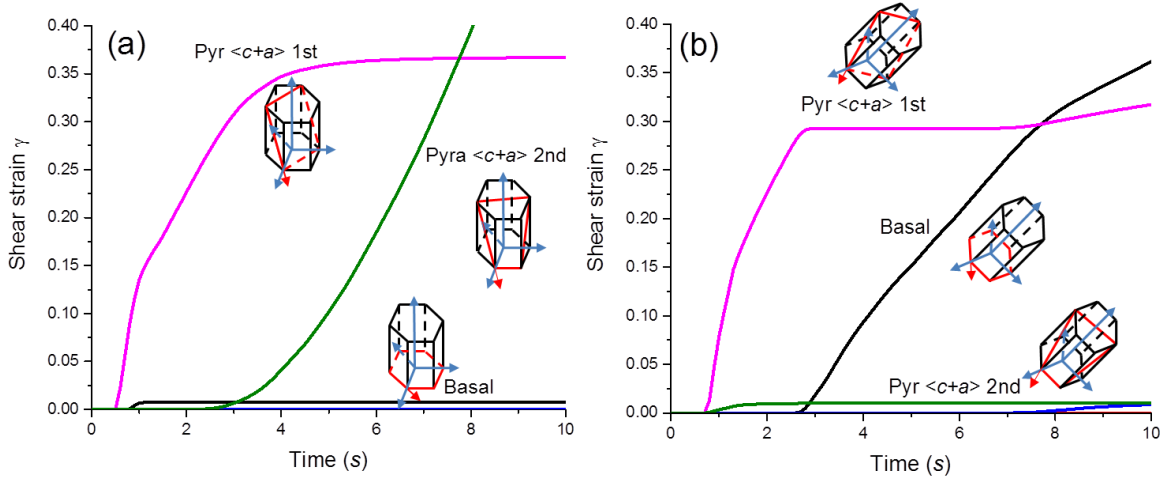


Figure 4 Shear strain evolution at the tip in (a) orientation 1 and (b) orientation 2

Next, we quantify the shear strains at the end of the loading step at locations 1-3 (Figure 5). Interestingly, the slip activation among all the locations in both orientation 1 and 2 favours the 1st order pyramidal $\langle c+a \rangle$ family, which indicates that it is the dominant slip system under the nanoindentation process. The slip activities in location 1 and location 2 behave similarly. This is due to crystal symmetry. Moderate activation of the basal family is observed in all locations in orientation 1 while that in orientation 2 is negligible. Also, little or no activation of prismatic and pyramidal $\langle a \rangle$ was observed in orientation 1, which agree with the general belief that these two families are harder to activate. However, if the crystallographic orientation and the loading condition are in favour (such as nanoindentation in orientation 2), the prismatic and pyramidal $\langle a \rangle$ could potentially be activated. Another observation is that there is moderate activation in 2nd order pyramidal $\langle c+a \rangle$ family at location 1 and 2 but not in location 3, which implies that this family is heavily dependent on the local orientation of the crystal or indenter geometry.

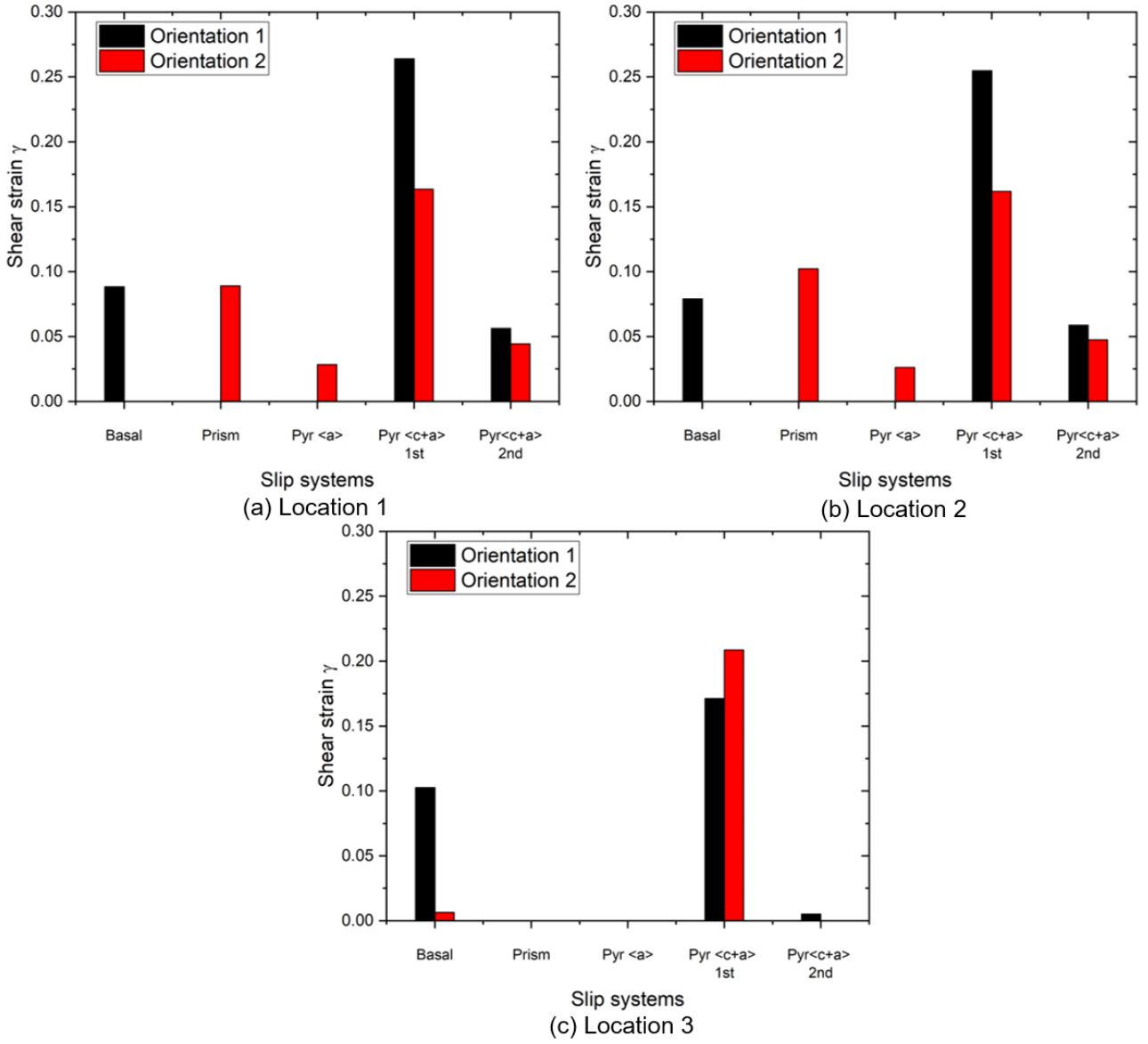


Figure 5 Shear strain of the five slip systems (which implies summation of slip on the entire family of the slip system) at the final step of loading at (a) location 1, (b) location 2 and (c) location 3.

4.3 Misorientation angle of the imprint

Here, we employ a concept of misorientation angle to quantify the variation of crystallographic orientation post-deformation. The misorientation angle can be used to quantify the variation in the orientation of crystalline material especially after localises deformation such as in micro-machining [24] and shear-band formation [19]. The misorientation angle is expressed as

$$\theta = \left| \cos^{-1} \left\{ \frac{\text{tr}(\mathbf{g}_A \mathbf{g}_B^{-1} - 1)}{2} \right\} \right| \quad (13)$$

where θ is the misorientation angle, \mathbf{g}_A and \mathbf{g}_B are the orientation matrices at chosen spatial location A and B, respectively. The reference configuration for calculating the misorientation angle was determined from the crystallographic structure before the deformation process. Figure 6 (a) and (b) show the contour plot of the residual imprint after the unloading step in orientation 1 and orientation 2, respectively. In orientation 1, we observe a similar pattern of the misorientation angle on all the three sides of the imprint due to crystal symmetry, while in orientation 2, the misorientation angle on one of the faces is more significant than the other two faces. To further study the difference of local deformation, a comparison of the variation of the misorientation angle along path X-Y for both orienta-

tions is shown in Fig. 6(c). The peak values of the variation of the crystallographic orientation were close to 21° in orientation 1 and 23° in orientation 2. Although the peak values were similar in both orientations, the locations of the peak and the misorientation pattern along the path X-Y were significantly different. We note that the simulations for these studies were identical with regard to mesh, boundary conditions and indenter geometry. This suggests that the difference in misorientation angle observed after deformation was solely due to the crystallographic orientation, which implies that different slip systems were activated in the two orientations.

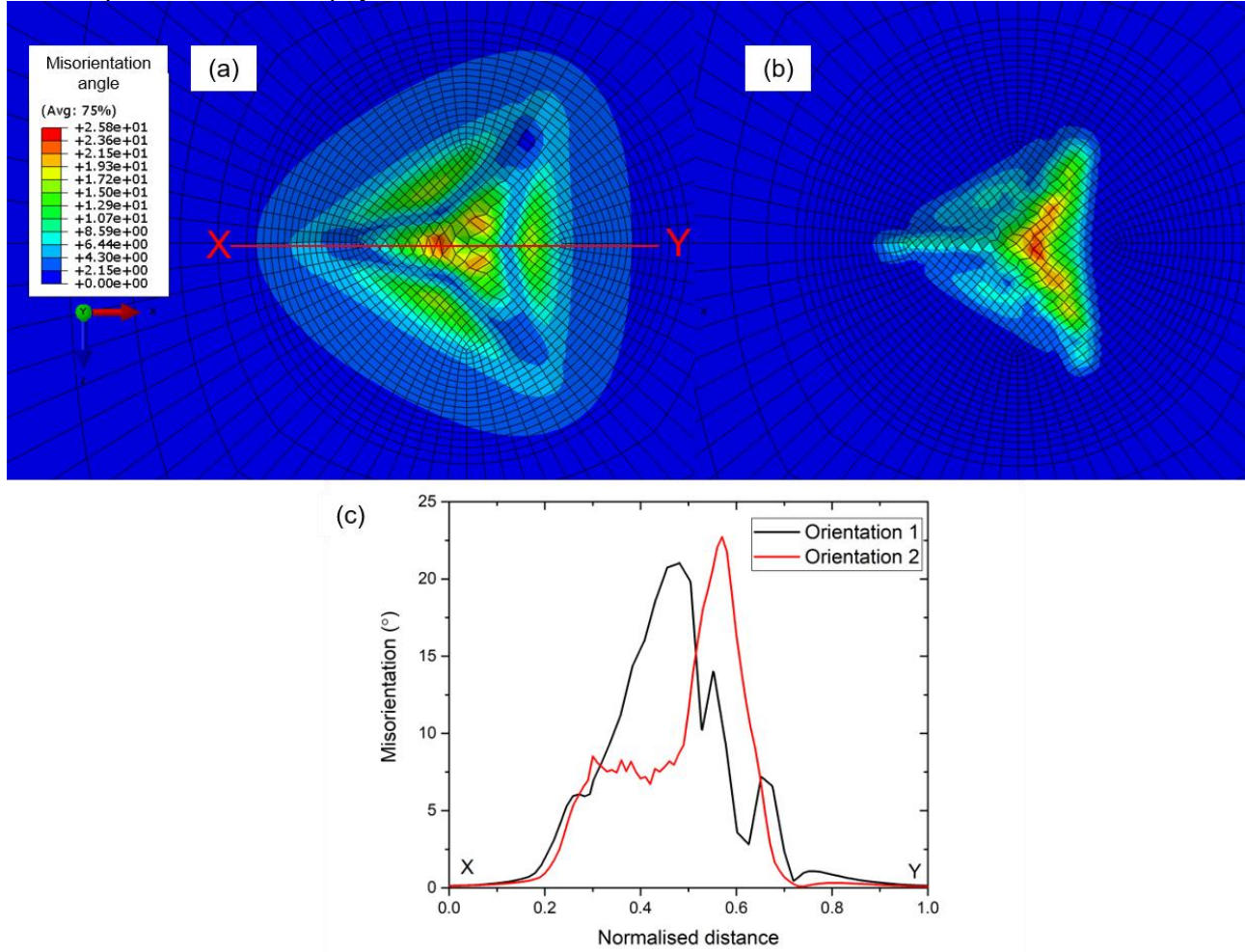


Figure 6 Contour plot of misorientation angle after unloading (a) orientation 1, (b) orientation 2 and (c) comparison of misorientation angle along path X-Y in orientation 1 and 2 as indicated in (a)

5. CONCLUSIONS

The nuances of slip system activation and evolution in 6H-SiC were discussed here. It is evident that the shear strain evolution in all the five slip systems directly under the indenter tip was present. The result indicates that the deformation is dominated by slip activation in 1st order pyramidal $\langle c+a \rangle$ family with potential activation of basal or 2nd order pyramidal $\langle c+a \rangle$ families depending on the crystallographic orientations. The slip activities along different faces on the nanoindentation imprint were also studied. The results support the claim that 1st order pyramidal $\langle c+a \rangle$ family dominates the deformation locally. Thus, we conclude that that slip activation induced by nanoindentation is complex, multi-slip dominated and not solely an effect of basal slip. In fact, pyramidal $\langle c+a \rangle$ systems contribute significantly to the deformation process and other slip systems may also contribute to the deformation locally depending on the crystallographic orientation and indenter geometry. Therefore considering all slip systems in predicting the deformation of 6H-SiC is crucial and must be incorporated in all predictive modelling of this material. Since indentation by its very nature is a strain gradient inducing deformation mode, it may be worthwhile to incorporate non-local gradient crystal plasticity formulations to account for strain-gradient effects to account for indentation size-effects. We shall study this in the future.

REFERENCES

- Kim, S., Choi, J., Jung, M., Joo, S. and Kim, S., "Silicon carbide-based hydrogen gas sensors for high-temperature applications," *Sensors*, **13**, pp. 13575–83. doi:10.3390/s131013575 (2013).
- Friedland, E., Hlatshwayo, T., and van der Berg, N., "Influence of radiation damage on diffusion of fission products in silicon carbide," *physica status solidi (c)*, **10**, pp. 208–215. doi:10.1002/pssc.201200457 (2013).
- Avincola, A. V., Grosse, M., Stegmaier, U., Steinbrueck, M., and Seifert, H. J., "Oxidation at high temperatures in steam atmosphere and quench of silicon carbide composites for nuclear application," *Nuclear Engineering and Design*, **295**, pp. 468–478. doi:10.1016/j.nucengdes.2015.10.002 (2015).
- Mehregany, M., and Zorman, C. A., "SiC MEMS: opportunities and challenges for applications in harsh environments," *Thin Solid Films*, **355**, pp. 518–524. doi:10.1016/S0257-8972(99)00374-6 (1999).
- Yin, L., Vancoille, E. Y. J., Ramesh, K., and Huang, H., "Surface characterization of 6H-SiC (0001) substrates in indentation and abrasive machining," *International Journal of Machine Tools and Manufacture*, **44**, pp. 607–615. doi:10.1016/j.ijmachtools.2003.12.006 (2004).
- Meng, B., Zhang, Y., and Zhang, F., "Material removal mechanism of 6H-SiC studied by nano-scratching with Berkovich indenter," *Applied Physics A*, **122**, pp. 247. doi:10.1007/s00339-016-9802-7 (2016).
- Morris, J. C., & Callahan, D. L. Origins of microplasticity in low-load scratching of silicon. *Journal of Materials Research*, **9**(11), pp. 2907–2913. <https://doi.org/10.1557/JMR.1994.2907> (1994).
- Wang, P., Ge, P., Bi, W., Liu, T., & Gao, Y. "Stress analysis in scratching of anisotropic single-crystal silicon carbide." *International Journal of Mechanical Sciences*, **141**, pp. 1–8. <https://doi.org/10.1016/j.ijmecsci.2018.03.042> (2018).
- Goel, S., Luo, X., Comley, P., Reuben, R. L., and Cox, A., "Brittle–ductile transition during diamond turning of single crystal silicon carbide," *International Journal of Machine Tools and Manufacture*, **65**, pp. 15–21. doi:10.1016/j.ijmachtools.2012.09.001 (2013).
- Mir, A., Luo, X., & Siddiq, A. Smooth particle hydrodynamics study of surface defect machining for diamond turning of silicon. *International Journal of Advanced Manufacturing Technology*, **88**(9–12), pp. 2461–2476. <https://doi.org/10.1007/s00170-016-8940-6> (2017).
- Patten, J., Gao, W., and Yasuto, K., "Ductile Regime Nanomachining of Single-Crystal Silicon Carbide," *Journal of Manufacturing Science and Engineering*, **127**, 522. doi:10.1115/1.1949614 (2005).
- Yan, J., Zhang, Z., and Kuriyagawa, T., "Mechanism for material removal in diamond turning of reaction-bonded silicon carbide," *International Journal of Machine Tools and Manufacture*, **49**, pp. 366–374. doi:10.1016/j.ijmachtools.2008.12.007 (2009).
- Xiao, G., To, S., and Zhang, G., "The mechanism of ductile deformation in ductile regime machining of 6H SiC. Computational Materials Science," **98**, pp. 178–188. doi:10.1016/j.commatsci.2014.10.045 (2015).
- Yan, J., Gai, X., and Harada, H. "Subsurface Damage of Single Crystalline Silicon Carbide in Nanoindentation Tests," *Journal of Nanoscience and Nanotechnology*, **10**, pp. 7808–7811. doi:10.1166/jnn.2010.2895 (2010).
- Page, T. F., Oliver, W. C., and McHargue, C. J., "The deformation behavior of ceramic crystals subjected to very low load nanoindentations," *Journal of Materials Research*, **7**, pp. 450–473. doi:10.1557/JMR.1992.0450 (1992).
- Page, T. F., Riester, L., and Hainsworth, S. V., "The Plasticity Response Of 6H-Sic and Related Isostructural Materials to Nanoindentation: Slip vs Densification," *MRS Proceedings*, **522**, pp. 113. doi:10.1557/PROC-522-113 (1998).
- Datye, A., Li, L., Zhang, W., Wei, Y., Gao, Y., and Pharr, G. M., "Extraction of Anisotropic Mechanical Properties From Nanoindentation of SiC-6H Single Crystals," *Journal of Applied Mechanics*, **83**, 091003. doi:10.1115/1.4033790 (2016).
- Pang, K. H., Tymicki, E., and Roy, A., "Indentation in single-crystal 6H silicon carbide: Experimental investigations and finite element analysis," *International Journal of Mechanical Sciences*, **144**. doi:10.1016/j.ijmecsci.2017.11.021 (2018).
- Zhou, R., Pang, K.-H. (Xavier), Bisht, A., Roy, A., Suwas, S., and Silberschmidt, V. V., "Modelling strain localization in Ti-6Al-4V at high loading rate: A phenomenological approach," *Philosophical Transactions of the Royal Society A: Mathematical, Physical and Engineering Sciences*. (2019). In press
- Liu, Q., Roy, A., and Silberschmidt, V. V., "Temperature-dependent crystal-plasticity model for magnesium: A bottom-up approach," *Mechanics of Materials*, **113**(Supplement C), pp. 44–56. doi:<https://doi.org/10.1016/j.mechmat.2017.07.008> (2017).
- Staroselsky, A., and Anand, L., "A constitutive model for hcp materials deforming by slip and twinning," *International Journal of Plasticity*, **19**, pp. 1843–1864. doi:10.1016/S0749-6419(03)00039-1 (2003).
- Gao, Y. F., Larson, B. C., Lee, J. H., Nicola, L., Tischler, J. Z., and Pharr, G. M., "Lattice Rotation Patterns and Strain Gradient Effects in Face-Centered-Cubic Single Crystals Under Spherical Indentation," *Journal of Applied Mechanics*, **82**, 061007. doi:10.1115/1.4030403 (2015).
- Liu, Q., Demiral, M., Roy, A., and Silberschmidt, V. V., "Modelling and Simulations of Nanoindentation in

- Single Crystals,” In *Applied Nanoindentation in Advanced Materials*, John Wiley and Sons Ltd., pp. 561–577. doi:10.1002/9781119084501.ch23 (2017).
24. Liu, Q., Roy, A., Tamura, S., Matsumura, T., and Silberschmidt, V. V., “Micro-cutting of single-crystal metal: Finite-element analysis of deformation and material removal,” *International Journal of Mechanical Sciences*, **118**, pp. 135–143. doi:10.1016/j.ijmecsci.2016.09.021 (2016).
 25. Huang, Y., A User-material Subroutine Incorporating Single Crystal Plasticity in the ABAQUS Finite Element Program. Harvard University (1991).
 26. Hutchinson, J. W., “Bounds and Self-Consistent Estimates for Creep of Polycrystalline Materials,” *Proceedings of the Royal Society of London A: Mathematical, Physical and Engineering Sciences*, **348**, (10 February 1976).
 27. Peirce, D., Asaro, R. J., and Needleman, A., “An analysis of nonuniform and localized deformation in ductile single crystals,” *Acta Metallurgica*, **30**, pp. 1087–1119. doi:10.1016/0001-6160(82)90005-0 (1982).
 28. Asaro, R. J., “Crystal Plasticity,” *Journal of Applied Mechanics*, **50**, pp. 921. doi:10.1115/1.3167205 (1983).
 29. Asaro, R. J., “Micromechanics of Crystals and Polycrystals,” *Advances in Applied Mechanics*, **23**, doi:10.1016/S0065-2156(08)70242-4 (1983).